


Research Article

Impact Dynamic Analysis and Rubber Impact-Resistant Design of a Launcher

Cunsheng Zhao and Bo Tong 

College of Naval Architecture and Ocean Engineering, Naval University of Engineering, Wuhan 430033, Hubei, China

Correspondence should be addressed to Bo Tong; tongbo19890712@126.com

Received 14 November 2022; Revised 19 December 2022; Accepted 24 December 2022; Published 7 January 2023

Academic Editor: R. Luo

Copyright © 2023 Cunsheng Zhao and Bo Tong. This is an open access article distributed under the Creative Commons Attribution License, which permits unrestricted use, distribution, and reproduction in any medium, provided the original work is properly cited.

To study the influence of the opening process of a naval ship's weapon launcher on the local strength of the impact-resistant structure, the load and inherent characteristics of the system were analyzed, a finite element dynamic model and theoretical Kelvin–Voigt single degree of the freedom system model were established, the dynamic response properties of the impact-resistant structure under an impact load were studied, and the impact spectrum of the system at different impact load durations was obtained. The results indicated that the first-order vibration period of the impact-resistant structure was much shorter than the impact load duration, and the dynamic amplification coefficient of the system was close to 1. Consequently, a theoretical model of a single degree of the freedom system was established, while the analytically derived displacement spectrum was consistent with the finite element calculation results. Therefore, the dynamic strength check of this impact-resistant structure could be treated as a static problem. According to the static calculation, the maximum stress of the structure occurred at the root of the base, which was 188.3 MPa, exceeds 0.3 times of the material yield stress specified in the military standard. To meet the military standard, a simplified collision model was established with the thickness of the rubber pad as the reference variable, the combined force on the bottom surface of the rubber pad was extracted, and the resulting equivalent displacement was calculated according to Hooke's law. The range of the rubber pad thickness was determined as $11.6 \text{ mm} < d < 12.5 \text{ mm}$ to meet the military standard and not affect the normal firing of the weapon.

1. Introduction

The impact resistance of naval ships has attracted increasing research attention as an important index to evaluate their vitality [1]. The transient noise caused by the impact force of a weapon launch can expose the position of submarines during wartime, which can have fatal consequences. Therefore, it is necessary to examine and improve the transient noise control technology to realize the combination of acoustic stealth and combat functionality [2, 3]. Lai et al. [4] and Kuang et al. [5] enhanced the hydraulic mechanism design of the lifting and closing device of a naval ship, successfully reducing the impact force of the drag reduction plate on the hull structure. Wang et al. [6] performed a finite element numerical simulation of the submarine cabin structure to obtain the law of impact spectrum

variation with mass and stiffness of naval ship equipment in different connection modes, revealing the limitations of the dynamic design analysis method (DDAM) commonly used for naval vessels. It is common to use rubber materials in military equipment to generate a considerable amount of internal friction during the deformation process, absorbing the kinetic energy of impact to reduce the transient impact force [7, 8]. Zhao et al. [9] established the constitutive relation of rubber buffer components through static and dynamic load experiment and analyzed the impact of rubber buffer component of a sniper grenade launcher on its firing performance using Adams software. Li et al. [10] applied finite element calculation and analysis to the impact problem presented by the projectile ejection device with a rubber cushion and examined its dynamic structural strength. Li [11] adopted the finite element method to establish a

mechanical model of a composite material launcher while analyzing and evaluating its dynamic performance in a launch state. Ravishankar et al. [12, 13] conducted finite element modeling for ballistic impact behavior of sandwich structures made of different composite materials, pointing out that the energy absorption capacity of glass-rubber-epoxy sandwich was highest among the natural rubber and glass-epoxy.

The rubber collision and impact-resistant structure is not limited to the military field but is also widely used in civil engineering. For example, using the finite element method, Yuan et al. [14] studied the influence of the rubber-damping layer thickness on the damping characteristics of rock arch structures under an explosion load. Liu et al. [15] designed a flexible box structure, an anticollision device for the bridge pier protection of ships. This device could effectively absorb a significant amount of impact energy, reduce the impact reaction force, improve the anticollision ability of vessels, protect the bridge and ship, and reduce losses due to accidents. Chen et al. [16] used the honeycomb structure composed of corrugated steel pipes as the anticollision structure of bridge piers, and verified the effectiveness of the design through test methods. Zeng et al. [17] calculated the dynamic response of train tracks. Xu et al. [18] used the finite element method and a genetic algorithm to optimize the energy absorption rate of the rubber ring buffer at the junction of a locomotive under impact load. Lu et al. [19] established a multidegree of the freedom dynamic model for the hinged floating structure with rubber cushion, and studied its hydrodynamic response, the results show that the strength of the rubber cushion designed meets the allowable stress of the material.

Wang et al. [20] studied the impact of aircraft landing on airborne equipment and analyzed the differences between the impact characteristics of two types of engines. Luo et al. [21] conducted numerical simulation on the dynamic characteristics of the shield tunnel under aircraft taxiing load to obtain a reasonable range of taxiing speed and tunnel depth.

Most of these studies utilized dynamic software to simplify and resolve the impact problem in the impact-resistant structures of large equipment according to their impact characteristics [22]. Based on this, and targeting the impact response of the drag reduction plate on the hull of the ship when the launching and closing device is opened, this study extracted the main vibration components during the impact response process to establish an effective mechanical model of a single degree of the freedom system. Furthermore, it combined theoretical analysis and finite element calculations, studied the load and dynamic response characteristics of the impact-resistant structure under impact load, and created the impact spectrum curves with different load times. In addition, a simplified finite element model was established based on the dynamic response characteristics, impact spectrum, and rubber material performance tests, while the rubber impact-resistant pad size was designed to meet the strength requirements. This study provides a new possibility for resolving the collision challenge presented by launchers.

2. The Dynamic Model Analysis of the Drag Reduction Plate of the Launcher

2.1. Impact Load Analysis. Figure 1 shows a schematic diagram of a naval ship launcher. The cover plate could be hydraulically opened, and the drag reduction plate, driven by the crank connection mechanism, could rotate while the stopper was attached to the hull. The drag reduction plate consumed kinetic energy via the collision stopper, and the angular velocity was reduced to zero to open the launcher in place. The drag reducer plate weighed about 300 kg. Since the stopper impact time was short, this could be regarded as the transient impact load on the stopper, with a contact area of 1200 mm². In order to avoid the stress singularity of the connection part and ensure the accuracy, the part of the hull structure connecting the impact-resistant structure is taken into account, and the connection part of the hull can be regarded as a fixed boundary. Figure 2 shows the size of the stopper and its base. This transient impact caused two types of damage. First, the significant short-term impact caused the dynamic response of the structure to exceed the yield strength, which could lead to local structural stress failure. Second, the significant transient vibration and noise caused by considerable impact force could easily expose the position and attack intention from the side.

To further examine the impact on the system, a 511F05 dynamic force sensor was installed at the impact location to test the force signal (Figure 3). The collected impact force-time history curve of the stopper is shown in Figure 4(a). After the impact force was restored to zero, it turned negative, indicating that the drag reduction plate rebounded after impacting the hull structure. Since the rebound disappeared within 3 s, and the maximum value of the rebound force was one order lower than the maximum value of the impact force, the collision could be described as in a completely inelastic state, that is, the rebound action did not require consideration [23]. Due to the short duration of the impact force, the impact load was approximated via the triangular load for theoretical analysis, as shown in Figure 4(b).

The triangular load can be described mathematically as follows:

$$F(t) = \begin{cases} \frac{F_0}{t_1}t, & 0 \leq t \leq t_1, \\ \frac{F_0}{t_2 - t_1}(t_2 - t), & t_1 < t \leq t_2, \end{cases} \quad (1)$$

where $F_0 = 15$ kN, $t_1 = 0.125$ s, and $t_2 = 0.635$ s.

2.2. Analysis of the Inherent System Characteristics and the Static Mechanics Calculation. The impact-resistant structure composed of the stopper and the base was considered the vibration system, while the connection between the bottom of the base and the hull was regarded as the fixed support. The free vibration of the structure was calculated via finite element software, using common carbon steel as the impact-

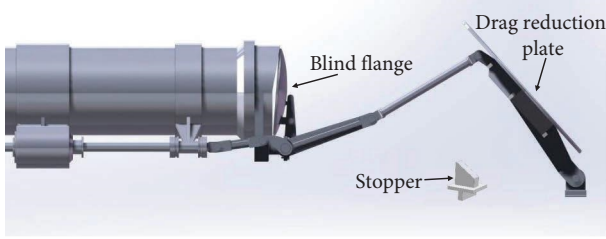


FIGURE 1: The structural diagram of the launcher.

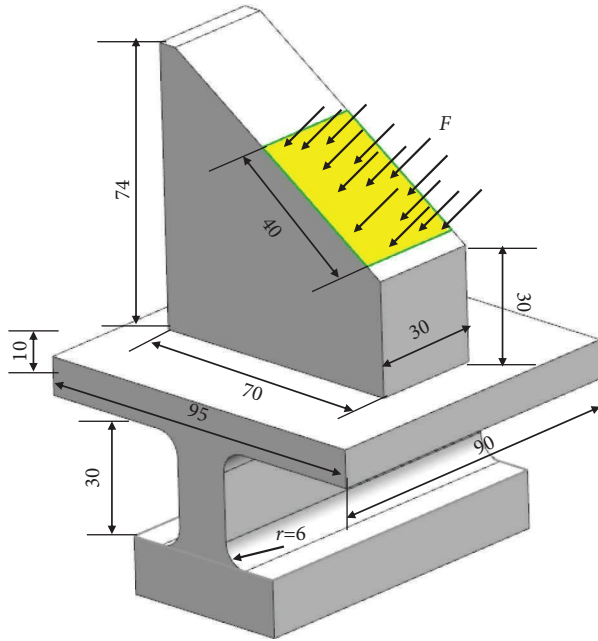


FIGURE 2: The dimensions of the stopper and base.



FIGURE 3: The dynamic force test.

resistant structure material, with an elastic modulus of 210 GPa, Poisson's ratio of 0.3, yield stress of 355 MPa, and a density of 7850 kg/m³. The geometric parameters are shown in Figure 2, and the finite element mesh is shown in Figure 5. The first-order natural frequency calculated by the finite

element method (FEM) was $f_1 = 993.02$ Hz, that is, the first-order vibration period was about 0.001 s. The impact load duration was much longer than the first-order vibration period of the system. Therefore, the vibration system will likely produce only first-order vibration at the impact force and can be treated as a single-degree-of-freedom system.

The static analysis of this system was performed using finite element software. A static force with a size of F_0 was applied to the force surface of the impact load of the stopper, while the center point of the dynamic load action surface was considered the equivalent displacement point. The deformation vector diagram is shown in Figure 6, with an equivalent displacement of $x_0 = 0.2$ mm. The equivalent stiffness and mass of the system were calculated according to the abovementioned expression of the first-order natural frequency was $f_1 = 1/2\pi\sqrt{k/m}$. The equivalent stiffness was $k = F_0/x_0 = 7.04 \times 10^7$ N/m, and the equivalent mass was $m = 1.81$ kg. After grid independence analysis, the maximum stress value and location are obtained by using the optimal mesh strategy with acceptable calculation speed and accuracy. As shown in Figure 7, the maximum stress occurred at the middle of the connection, which is 188.3 MPa.

2.3. The Analytical Solution and Finite Element Analysis of the Impact Vibration Response. The dynamics analysis in this paper is likely to exhibit only low modal response. For this case, the use of implicit unconditional stabilization algorithms is usually preferred over conditional stabilization algorithms [24]. Therefore, an implicit direct algorithm was used to perform the matrix iteration using the Newton–Raphson method to ensure calculation accuracy. Eight time steps of 0.12588 ms were set in each vibration period, respectively. The computing platform consisted of four cores and a 3.2 GHz processor, while the computing time was 3.5 h. The center point of the action surface of the force was considered the reference point to calculate its acceleration curve with time, as shown in Figure 8. Due to the influence of structural damping, the variation in the acceleration response caused by the impact was attenuated in three time periods ($0 < t < 0.125$ s, $0.125 < t < 0.635$ s, and $0.635 < t < 1$ s). In addition, during the first two periods, the structure was subjected to different external loads, while no external forces were evident in the third period. Therefore, the three periods showed different attenuation trends.

Fourier transform analysis was performed on the vibration curves of the three stages (as shown in Figure 9), showing that the system only has one resonant frequency point, namely 993.01 Hz, which is highly consistent with the first-order natural frequency (993.02 Hz), of the impact-resistant structure and verifies the accuracy of the implicit direct calculation method. It also indicated that the impact response analysis of the stopper and base system could be considered a Kelvin–Voigt single-degree-of-freedom model under this transient impact load, as shown in Figure 10, where c represented the damping coefficient of the system.

The HHT [24] integration algorithm is adopted in the implicit solution method, which has no numerical dissipation for the low frequency response [25]. As shown in

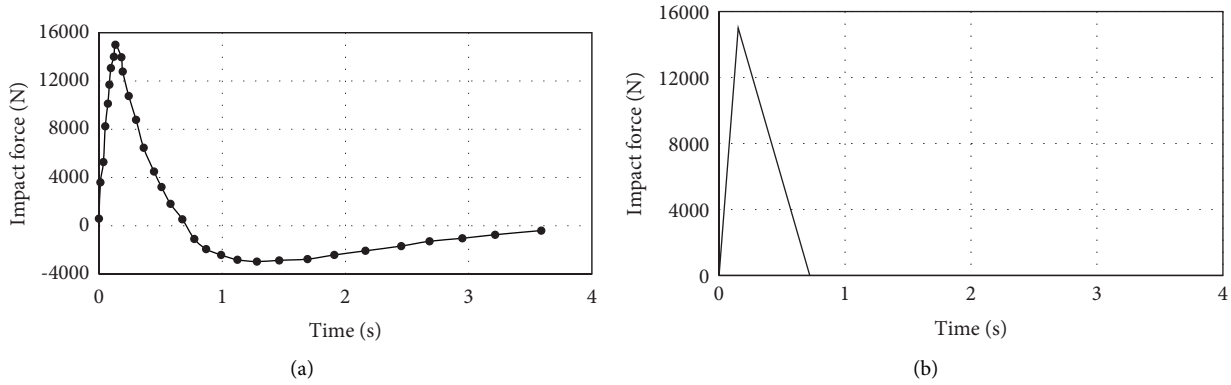


FIGURE 4: The impact force-time history curve of the stopper: (a) measured forced signal; (b) simplified impact load.

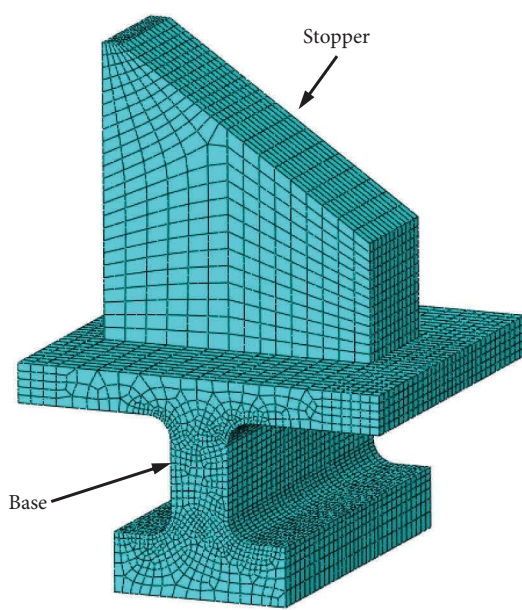


FIGURE 5: The finite element mesh of the impact-resistant structure.

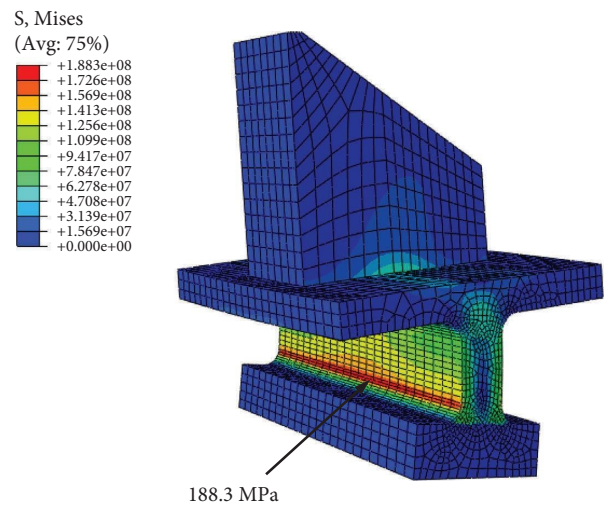


FIGURE 7: The stress distribution of the impact-resistant structure under static force.

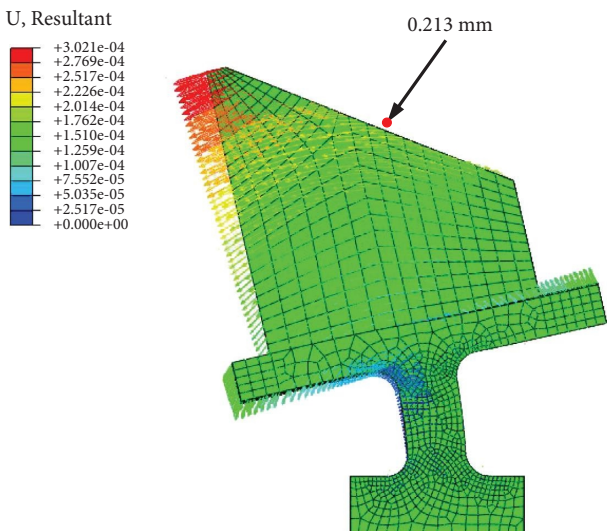


FIGURE 6: The deformation vector diagram of the impact-resistant structure under static force.

Figure 11, the results of finite element calculation show that the dissipated energy ALLVD is always zero with time, and the total strain energy ALLIE reaches the peak when the impact force is at its maximum, which exactly verifies the above views of the literature [25]. Therefore, the real structural damping coefficient can be extracted from the attenuation curve of acceleration by the FEM model.

Amplitude attenuation curves, A1, A2, and A3, are fitted in Figure 12, which shows that the attenuation coefficients of the three curves were exceedingly close. Due to the external force interference in A1 and A2 stages, the curve A3 was used to calculate the damping coefficient of the system.

According to the attenuation law of free vibration [26], $\zeta\omega_n = 13.23$, where ζ is the damping ratio; $\zeta = c/2m\omega_n$; and ω_n is the natural circular frequency $\omega_n = 2\pi f_1 = 6239.3\text{rad/s}$. Therefore, the damping ratio is $\zeta = 0.0021$ and the damping coefficient is $c = 47.9\text{N/m}\cdot\text{s}^{-1}$.

Under the triangular load in equation (1), the displacement response of the damped single-degree-of-freedom system is solved according to the Duammil integral. The system response under the action of the microimpulse $F(\tau)d\tau$ is as follows:

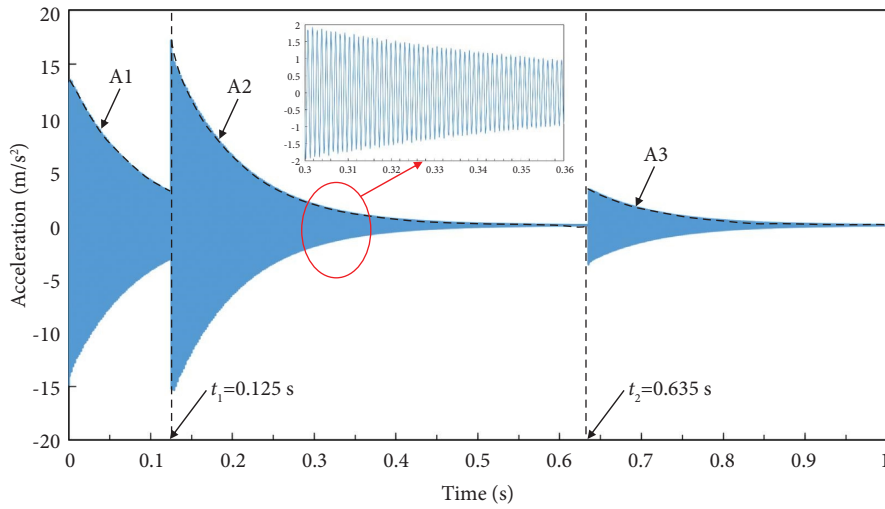


FIGURE 8: The acceleration response curve by the FEM.

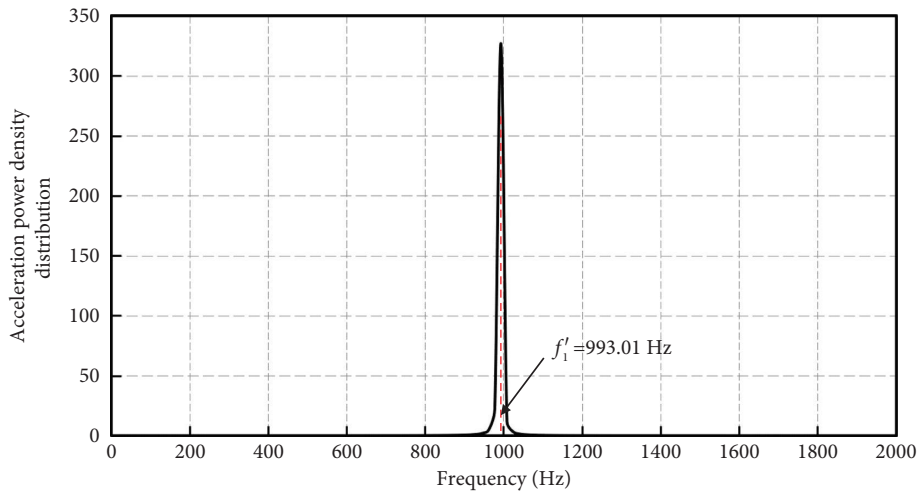


FIGURE 9: Fourier transform of acceleration.

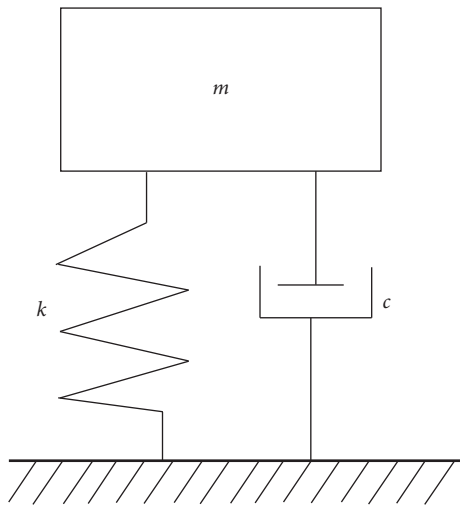


FIGURE 10: The Kelvin-Voigt single-degree-of-freedom model.

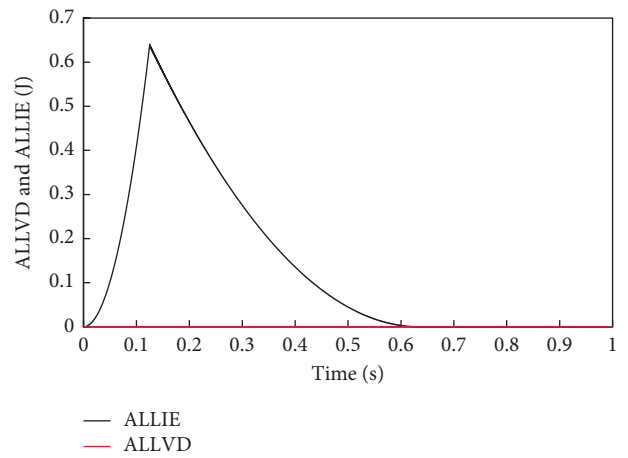


FIGURE 11: ALLVD-time and ALLIE-time curves.

$$dx = \frac{F(\tau)}{m\omega_d} e^{-\zeta\omega_n(t-\tau)} \sin \omega_d(t-\tau) d\tau. \quad (2)$$

Then, in the first stage ($0 < t < t_1$), we have

$$x(t) = \int_0^t \frac{F_0\tau}{m\omega_d t_1} e^{-\zeta\omega_n(t-\tau)} \sin \omega_d(t-\tau) d\tau. \quad (3)$$

$$x(t) = \frac{F_0 e^{-\zeta\omega_n t}}{m t_1 \omega_n^3 \sqrt{1-\zeta^2}} \left[(\omega_n t - 2\zeta) \sqrt{1-\zeta^2} e^{\zeta\omega_n t} + 2\zeta \sqrt{1-\zeta^2} \cos(\sqrt{1-\zeta^2} \omega_n t) - (1-2\zeta^2) \sin(\sqrt{1-\zeta^2} \omega_n t) \right]. \quad (4)$$

Since ζ ($\zeta = 0.$) is a minimum value, both $\sqrt{1-\zeta^2}$ and $1-2\zeta^2$ are approximately equal to 1. Equation (4) can be simplified as follows:

$$x(t) = \frac{F_0 e^{-\zeta\omega_n t}}{k t_1 \omega_n} \left[(\omega_n t - 2\zeta) e^{\zeta\omega_n t} + 2\zeta \cos \omega_n t - \sin \omega_n t \right]. \quad (5)$$

In the second stage, ($t_1 < t < t_2$), there are

$$x(t) = \int_0^{t_1} \frac{F_0\tau}{m\omega_d t_1} e^{-\zeta\omega_n(t-\tau)} \sin \omega_d(t-\tau) d\tau + \int_{t_1}^t \frac{1}{m\omega_d} \frac{F_0}{t_2-t_1} (t_2-\tau) e^{-\zeta\omega_n(t-\tau)} \sin \omega_d(t-\tau) d\tau. \quad (6)$$

The equation was integrated to obtain the following:

$$x(t) = \frac{F_0 e^{-\zeta\omega_n t}}{m\omega_n^3 t_1 (t_1-t_2) \sqrt{1-\zeta^2}} t_1 \sqrt{1-\zeta^2} e^{\zeta\omega_n t} (\omega_n t - \omega_n t_2 - 2\zeta) + 2(t_1-t_2)\zeta \sqrt{1-\zeta^2} \cos(\sqrt{1-\zeta^2} \omega_n t) + 2t_2\zeta \sqrt{1-\zeta^2} e^{\zeta\omega_n t_1} \cos[\sqrt{1-\zeta^2} \omega_n(t-t_1)] + (1-2\zeta^2)(t_2-t_1) \sin(\sqrt{1-\zeta^2} \omega_n t) + t_2 e^{\zeta\omega_n t_1} (2\zeta^2-1) \sin[\sqrt{1-\zeta^2} \omega_n(t-t_1)]. \quad (7)$$

Since ζ^2 ($\zeta = 0.0021$) is a tiny value, both $\sqrt{1-\zeta^2}$ and $1-2\zeta^2$ are approximately equal to 1. Equation (7) can be simplified as follows:

The equation mentioned above was integrated to obtain the following:

$$x(t) = \frac{F_0 e^{-\zeta\omega_n t}}{k\omega_n t_1 (t_1-t_2)} t_1 e^{\zeta\omega_n t} (\omega_n t - \omega_n t_2 - 2\zeta) + 2(t_1-t_2)\zeta \cos \omega_n t + 2t_2\zeta e^{\zeta\omega_n t_1} \cos[\omega_n(t-t_1)] + (t_2-t_1) \sin \omega_n t - t_2 e^{\zeta\omega_n t_1} \sin[\omega_n(t-t_1)]. \quad (8)$$

In the third stage ($t > t_2$), there is

$$x(t) = \int_0^{t_1} \frac{F_0\tau}{m\omega_d t_1} e^{-\zeta\omega_n(t-\tau)} \sin \omega_d(t-\tau) d\tau + \int_{t_1}^{t_2} \frac{1}{m\omega_d} \frac{F_0}{t_2-t_1} (t_2-\tau) e^{-\zeta\omega_n(t-\tau)} \sin \omega_d(t-\tau) d\tau. \quad (9)$$

The equation mentioned above was integrated and simplified to obtain the following:

$$x(t) = \frac{F_0 e^{-\zeta\omega_n t}}{k\omega_n t_1 (t_1-t_2)} 2(t_1-t_2)\zeta \cos \omega_n t + 2t_2\zeta e^{\zeta\omega_n t_1} \cos \omega_n(t-t_1) - 2t_1\zeta e^{\zeta\omega_n t_2} \cos \omega_n(t-t_2) + (t_2-t_1) \sin \omega_n t - t_2 e^{\zeta\omega_n t_1} \sin \omega_n(t-t_1) + t_1 e^{\zeta\omega_n t_2} \sin \omega_n(t-t_2). \quad (10)$$

After solving the equation mentioned above, the response of the single-degree-of-freedom system under the impact load can be expressed as follows:

$$x(t) = \begin{cases} x_{st} \left(\frac{t}{t_1} - \frac{2\zeta}{t_1 \omega_n} \right) + x_{st} \frac{e^{-\zeta \omega_n t}}{t_1 \omega_n} [2\zeta \cos \omega_n t - \sin \omega_n t], & 0 \leq t \leq t_1, \\ \frac{x_{st}}{\omega_n (t_1 - t_2)} (\omega_n t - \omega_n t_2 - 2\zeta) + x_{st} \frac{2\zeta e^{-\zeta \omega_n t}}{\omega_n t_1} \cos \omega_n t - x_{st} \frac{e^{-\zeta \omega_n t}}{\omega_n t_1} \sin \omega_n t, & t_1 < t \leq t_2, \\ + x_{st} \frac{2t_2 \zeta}{\omega_n t_1 (t_1 - t_2)} \cos [\omega_n (t - t_1)] - x_{st} \frac{t_2}{\omega_n t_1 (t_1 - t_2)} \sin [\omega_n (t - t_1)], & \\ x_{st} \frac{2\zeta e^{-\zeta \omega_n t}}{\omega_n t_1} \cos \omega_n t + x_{st} \frac{2t_2 \zeta}{\omega_n t_1 (t_1 - t_2)} e^{\zeta \omega_n (t_1 - t)} \cos [\omega_n (t - t_1)] - x_{st} \frac{2\zeta}{\omega_n (t_1 - t_2)} e^{\zeta \omega_n (t_2 - t)} \cos [\omega_n (t - t_2)], & t > t_2, \\ -x_{st} \frac{e^{-\zeta \omega_n t}}{\omega_n t_1} \sin \omega_n t - x_{st} \frac{t_2}{\omega_n t_1 (t_1 - t_2)} e^{\zeta \omega_n (t_1 - t)} \sin [\omega_n (t - t_1)] + x_{st} \frac{1}{\omega_n (t_1 - t_2)} e^{\zeta \omega_n (t_2 - t)} \sin [\omega_n (t - t_2)], & \end{cases} \quad (11)$$

where x_{st} is the static displacement under static load F_0 , and $x_{st} = F_0/k$. The analytical solution of displacement on the center point (equivalent displacement point) of the stopper contact surface under impact load was compared with the finite element numerical solution, as shown in Figure 13.

The trend of displacement variation with time derived by the Kelvin–Voigt single-degree-of-freedom model is highly consistent with that by the finite element implicit solution, and the maximum displacement obtained by both methods occurs at 0.125 seconds, with a difference of 2.3%, which verifies the accuracy of the theoretical model.

2.4. Analysis of the Influence of the Excitation Duration on the Dynamic Response of the System. The natural vibrational circular frequency of the system was $\omega_n = 6239.3$ rad/s, and the natural period was $T \approx 0.001$ s. When the excitation force was applied to the system as a dynamic load, it produced a certain dynamic load effect. Assuming that the ratio of the rising time t_1 and the falling time $t_2 - t_1$ of the exciting force was certain, then $t_2 - t_1/t_1 = 0.635 - 0.125/0.125 = 4.08$, while the maximum change law value of the dynamic system response at an excitation duration t_2/T ratio and the first-order vibration period T of the system were examined as variables. Take the ratio of maximum displacement to static displacement $\alpha = x_{\max}/x_{st}$ as the ordinate and t_2/T as the abscissa to draw the impact spectrum curve under dynamic load. The calculation results are shown in Figure 14. When t_2/T approached zero, the dynamic amplification coefficient α approached zero; when $t_2/T = 1.45$, α reached the maximum value of 1.7; and when t_2/T exceeded 5, the dynamic amplification coefficient α gradually tended toward 1. When the load duration is much smaller than the first-order vi-

bration period of the system, that is, t_2/T tends to zero, in other words, the excitation frequency is much larger than the first-order natural frequency of the system, the broadband response of the vibrational system may be excited, it cannot be regarded as a single-degree-of-freedom system. Therefore, the impact spectrum curve is not considered in the range when t_2/T is much less than 1.

The duration ratio t_2/T of the impact load on the stopper and the base to the natural vibration period of the system studied in this study is 577, which is far greater than 5. Therefore, the dynamic displacement of the stopper tended to the static displacement, that is, the impact load has no amplification effect on the system response. Since the maximum stress was directly related to the structural deformation, the deformation and stress distribution of the structure under the transient impact load was regarded as the deformation under static load. According to the calculation results obtained in Section 2.2, the maximum stress of the structure was 188.3 MPa, which occurred at the middle of the connection between the base and the hull.

Therefore, although the impact load did not dynamically amplify the system, according to the design specifications GJB/Z 21A-2001, the maximum generated stress still exceeded the allowable stress value of $[\sigma_c] = 0.3 \times 355 \text{ MPa} = 106.5 \text{ MPa}$. Consequently, laying rubber impact-resistant mats on the impact surface of the stopper to reduce the transient impact force is commonly used in engineering to reduce vibration and avoid local stress excess. The impact load generated by the rigid contact between the drag reduction plate and the stopper verified that the dynamic amplification factor equaled 1. According to the law of the impact spectrum presented in Figure 14, the t_2/T ratio increased after the rubber pads were laid, and the dynamic amplification factor was closer to 1, which could still be regarded as a static problem.

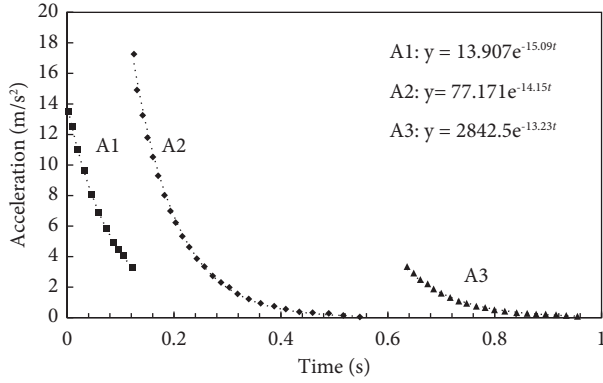


FIGURE 12: Fitting curves of amplitude attenuation at different stages.

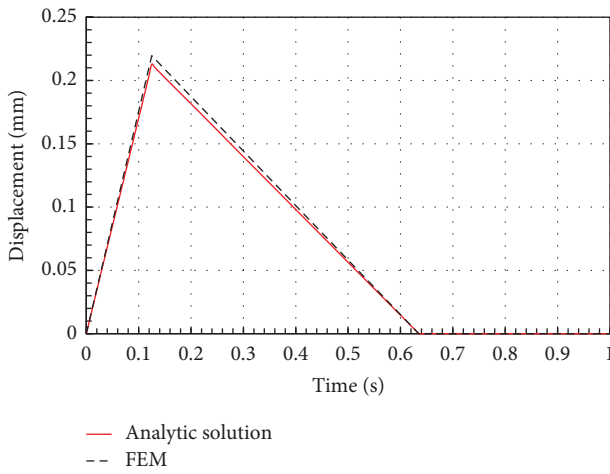


FIGURE 13: A comparison of displacement on the center point between the analytical solution and finite element solution.

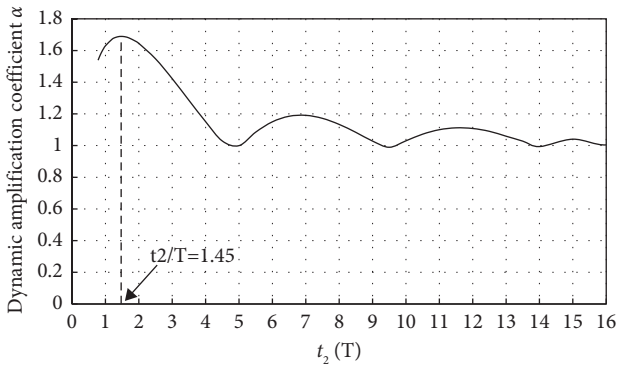


FIGURE 14: The impact spectrum.

3. The Rubber Impact-Resistant Mat Size Design

Since the impact response in this paper was a linear dynamic problem, the linear relationship between the displacement and stress of the stopper could be established. The force and deformation of the stopper conformed to Hooke's law, and the maximum stress caused by unit deformation was as follows:

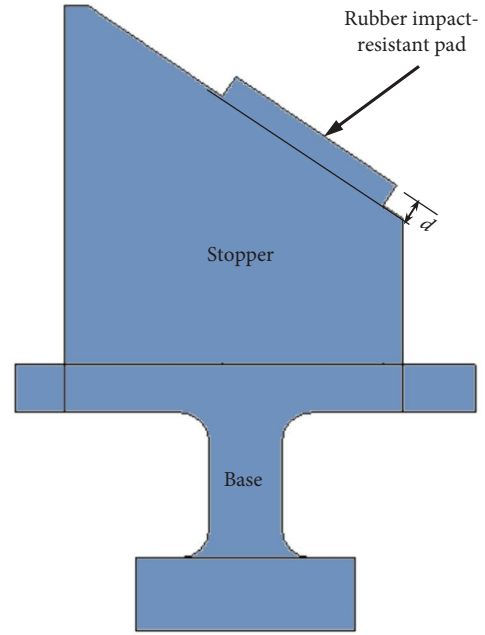


FIGURE 15: Installation position of the rubber impact-resistant pad.

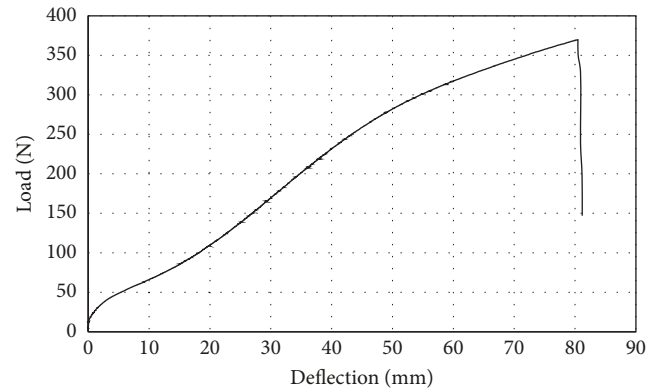


FIGURE 16: The "load-deflection" curve.

$$q = \frac{188.3 \text{ MPa}}{0.213 \text{ mm}} = 884.04 \frac{\text{MPa}}{\text{mm}}. \quad (12)$$

Then, on the condition that the vibration system composed of the stopper and the base met the allowable stress scale, the allowable displacement of the equivalent displacement point on the stopper was as follows:

$$x_c = \frac{\sigma_c}{q} = 0.12 \text{ mm}. \quad (13)$$

After the rubber pad was laid on the surface of the stopper, as shown in Figure 15, the bottom area of the rubber block was the same as the contact area between the drag reduction plate and the stopper, which was $A = 1200 \text{ mm}^2$. A thicker rubber block d absorbed more impact kinetic energy. However, if the rubber was too thick, the height of the drag reduction plate increased after it was opened and in place, possibly affecting the launching channel of the

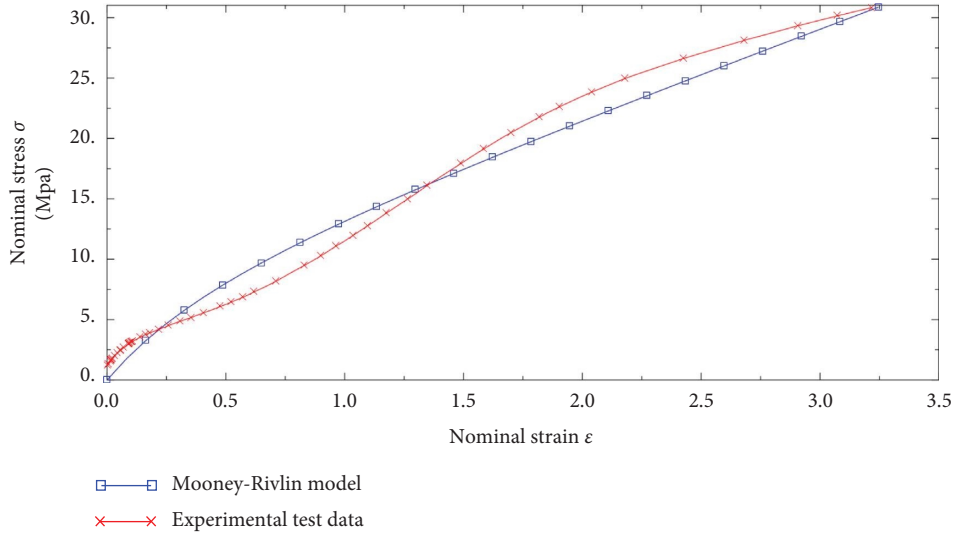


FIGURE 17: The nominal stress-strain curve.

weapon. After the drag reduction plate is opened and in place, the height of the rubber pad should be less than 5 mm to ensure the normal launch of the weapon.

3.1. Acquisition of the Property Parameters of the Rubber Materials. This study installed a rubber impact-resistant mat on the surface of the stopper. Because the mass of the drag reduction plate of the launcher was relatively large and the momenta of the contact with the stopper were substantial, a rubber material with a Shore hardness of 65 and density of 1630 kg/m^3 was selected while comprehensively considering its deformation potential energy and impact resistance.

To accurately describe the mechanical properties of the rubber material and facilitate calculation and analysis, dumbbell-shaped rubber specimens were created, and their tensile capacity was tested according to the determination procedures of GB/T528-2009. Specimen length $l = 25 \text{ mm}$, width $b = 6 \text{ mm}$, and thickness $d = 2 \text{ mm}$. The loading force at both ends of the specimen varied with the elongation, as shown in Figure 16. The axial force and deformation were transformed to obtain the nominal stress ($\sigma = F/bd$, where F is the axial force) and the nominal strain ($\varepsilon = z/l$, where z is the deformation). The stress-strain curve obtained by the experiment was fitted using the Mooney–Rivlin model on the finite element calculation platform ABAQUS, yielding an excellent general consistency, as shown in Figure 17. The C_{10} and C_{01} values of the Mooney–Rivlin constants were $3.62 \times 10^6 \text{ Pa}$ and $0.26 \times 10^6 \text{ Pa}$.

3.2. The Finite Element Analysis of the Simplified “Rubber Impact-Resistant Mat + Collider” Model. The reasonable thickness of the rubber impact-resistant mat was determined via finite element analysis after obtaining the material property parameters. The impact process fulfilled the conservation of the momentum, while the integration of the impact load presented in Section 2.1 over time yielded an impulse of $I = 4762.5 \text{ kg}\cdot\text{s}$. Actual ship measurements

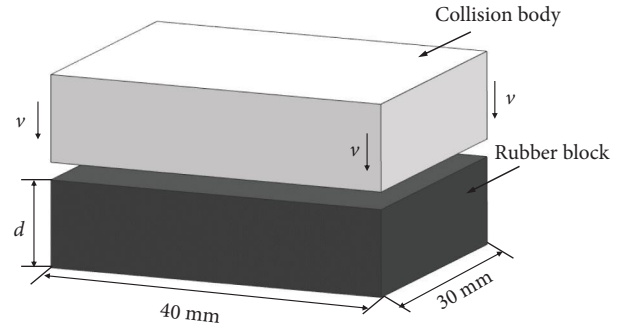


FIGURE 18: The collision model.

revealed that when the drag reduction plate collided with the stopper, the linear velocity of the drag reduction plate was $V_0 = 0.438 \text{ m/s}$. Therefore, the effective mass of the collision was $m_0 = 10873.3 \text{ kg}$. In the finite element calculation, the actual geometric size of the collider did not need to be expressed, requiring only the unstructured mass m_0 and initial velocity V_0 . The collision mechanics model is shown in Figure 18. At $40 \text{ mm} \times 30 \text{ mm}$, the bottom area of the collider and rubber block was the same, while the bottom of the rubber block was fixed. The finite element calculation defined the tangential frictionless and normal elastic contact, while a display algorithm was adopted, with a calculation and analysis time of 0.02 s, a quadcore CPU, a main frequency processor of 3.2 GHz, and a calculation time of 63 s.

Rubber blocks of different thicknesses were selected for the finite element calculation, while the maximum resultant force on the contact surface between the rubber blocks and the stopper was extracted, as shown in Table 1. The rubber impact-resistant mat absorbed more impact kinetic energy as the rubber pad thickness increased, while the force transferred to the stopper gradually decreased. However, when the thickness exceeded 12.5 mm, the decreasing trend diminished. The power was divided by the equivalent stiffness k of the system consisting of the stopper and the

TABLE 1: The calculation results of the force and equivalent displacement at different rubber block thicknesses.

Rubber block thickness (mm)	Forces on the bottom (N)	Equivalent displacement of the stopper (mm)
5	12318	0.167
7.5	11452.2	0.155
10	9736.7	0.132
12.5	8610.5	0.117
15	8344	0.113
17.5	8324	0.112

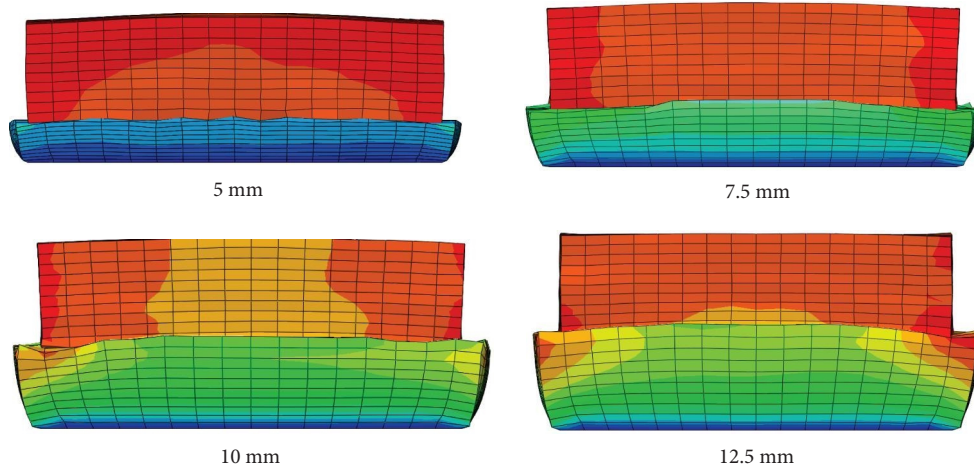


FIGURE 19: Displacement nephogram of rubber impact pads with different thicknesses at maximum deformation.

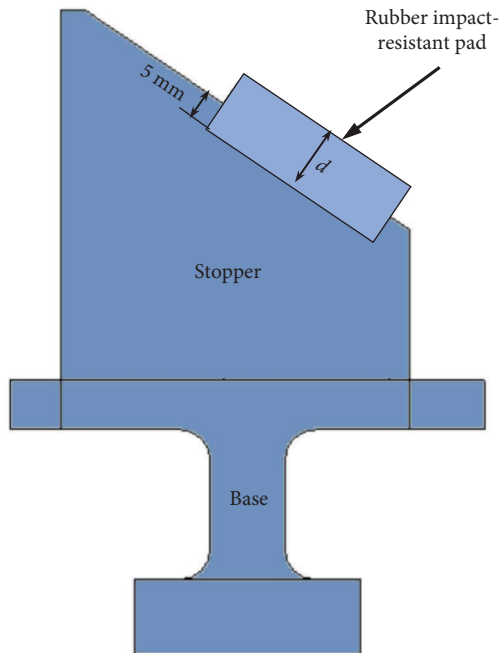


FIGURE 20: Assembly diagram of the rubber impact pad.

base according to Hooke's law to obtain the equivalent displacement at the center of the force surface. Furthermore, when the thickness exceeded 12.5 mm, the equivalent displacement was below the allowable displacement of 0.12 mm. Consequently, the equivalent displacement of the

stopper with a rubber thickness of 11.6 mm was equal to the permissible displacement by interpolation. Therefore, in order to meet the requirements of the design specifications, the thickness of the rubber impact-resistant mat laid on the stopper should exceed 11.6 mm. Figure 19 shows the displacement clouds of the four impact-resistant pads at maximum deformation. Meanwhile, the deformation rates of the rubber impact-resistant pad with different thicknesses in the thickness direction were all about 20%.

To satisfy the requirement of a rubber pad thickness below 5 mm after opening the drag reduction plate in place, that is, the height of the portion exceeding the stopper should be less than 5 mm, it is compressed. On condition that the stopper stiffness was not affected, a groove with a depth of 5 mm was added downward along the normal direction of the contact surface, as shown in Figure 20. Therefore, according to the 20% rubber deformation rate calculation, the thickness of the rubber mat should be less than 12.5 mm to meet the requirements. In summary, the thickness of the rubber impact mat should be $11.6 \text{ mm} < d < 12.5 \text{ mm}$.

4. Conclusions

This paper combines theoretical derivation and finite element analysis to examine the load and dynamic response characteristics of the impact-resistant structure of the launching and closing device of a certain type of weapon under an impact load. The size design of the rubber impact-resistant mat is accomplished based on these characteristics, and the conclusions are drawn as follows:

- (1) The first-order vibration period (0.001 s) of the impact-resistant structure consisting of the stopper and the base is much lower than the duration of the impact load. Therefore, the system only produces low-order vibration deformation under the impact load, which is verified via highly accurate implicit finite element dynamic calculations. The damping coefficient of the structure is obtained according to the displacement response attenuation curve, while the equivalent stiffness of the first-order vibration is obtained through static calculation.
- (2) Since the stopper and base of the impact-resistant structure under the impact load only exhibit first-order vibration deformation, the dynamic response analysis is considered a Kelvin–Voigt single-degree-of-freedom model. Consequently, the analytical solution of the displacement response of the single-degree-of-freedom system is derived, and the accuracy of the theoretical derivation is verified via comparison with the finite element results.
- (3) The impact spectrum curve of the system at different impact load duration is obtained according to the theoretical formula. For both the rigid and flexible contact containing rubber mat, the dynamic amplification coefficient is close to 1, the stress and deformation of the stopper is in accordance with Hooke's law, and the local strength can be checked as a statics issue, which greatly reduces the computational cost.
- (4) A simplified collision model is established for rubber pads with different thicknesses, followed by finite element calculations. According to Hooke's law, a rubber mat thickness range of $11.6 \text{ mm} < d < 12.5 \text{ mm}$ adequately meets the specification requirements for a normal weapon's launch.

Data Availability

The data used to support the findings of this study are included within the article.

Conflicts of Interest

The authors declare that they have no conflicts of interest.

Acknowledgments

This research was supported by the Military Scientific Research Project of Naval Armaments Department (No. 425315548).

References

- [1] L. Liu, *Research on Direct Analysis Approach for Static and Dynamic Response of a Floating Raft Isolation System*, Huazhong University of Science and Technology, Wuhan, China, 2018.
- [2] J. Zhou, N. Qin, and Y. Yin, "Simulation research on optimization of submarine underwater launcher reducing noise by decreasing power," *Computer Simulation*, vol. 36, no. 1, pp. 19–22+28, 2019.
- [3] X. Meng, G. Xiao, and H. Chen, "Review of the present situation and development of acoustic stealth technology for submarines abroad," *Ship Science and Technology*, vol. 33, no. 11, pp. 135–139, 2011.
- [4] H. Lai, J. Lou, and J. Sun, "Simulation and optimization of the opening and closing device on ships based on Adams and Amesim," *Chinese Journal of Ship Research*, vol. 9, no. 3, pp. 105–108+122, 2014.
- [5] Q. Kuang, Z. Zhang, and S. Zhu, "Analysis of cylinder buffering device's structure parameters to buffering performance effects," *Ship Science and Technology*, vol. 42, no. 3, pp. 132–136, 2020.
- [6] X. Wang, X. Li, and X. Ma, "Numerical analysis on spectrum dip characteristics of shock response spectrum of submarine equipment," *Chinese Journal of Ship Research*, vol. 14, no. 3, pp. 31–37, 2019.
- [7] X. Li, H. Mao, K. Xu, and C. Miao, "A SHPB experimental study on dynamic mechanical property of high-damping rubber," *Shock and Vibration*, vol. 2018, Article ID 3128268, 10 pages, 2018.
- [8] Y. Zou, C. Xiong, J. Yin et al., "Research on the dynamic mechanical properties and constitutive model of metal rubber under impact loading," *Materials Research Express*, vol. 8, no. 4, Article ID 046503, 15 pages, 2021.
- [9] P. Zhao, R. Wang, and Y. Li, "Effects of rubber buffer unit on launch performance of a sniper grenade launcher," *Journal of Vibration and Shock*, vol. 37, no. 23, pp. 241–246, 2018.
- [10] S. Li, G. Jiang, and H. Wang, "Collision finite element analysis of the jacking shells device with rubber cushion," *Applied Science and Technology*, vol. 41, no. 1, pp. 75–79, 2014.
- [11] H. Li, "Evaluation of the strength characteristics of a certain type of reinforced composite material launch tube," *Journal of Naval Aviation University*, vol. 37, no. 2, pp. 217–223, 2022.
- [12] K. S. Ravishankar, K. Ravishankar, and S. Kulkarni, "Ballistic impact study on jute-epoxy and natural rubber sandwich composites," *Materials Today Proceedings*, vol. 5, no. 2, pp. 6916–6923, 2018.
- [13] R. Sangamesh, H. Shivashankar, K. S. Ravishankar, and S. Kulkarni, "Study on ballistic characteristics of glass-epoxy-rubber sandwiches," *Materials Science Forum*, vol. 978, pp. 245–249, 2020.
- [14] Y. Yuan, H. Sun, Z. Chen, W. Zhang, and W. Xia, "Analysis of the damping effect of rubber damping layer under explosive load IOP Conference Series: earth and Environmental Science," *IOP Conference Series: Earth and Environmental Science*, vol. 669, no. 1, p. 012010, Article ID 012010, 2021.
- [15] J. Liu, J. Cao, and B. Sun, "The Design of dual-box pier anticollision device based on rubber cushion," *Applied Mechanics and Materials*, Trans Tech Publications Ltd, vol. 201, pp. 640–644, 2012.
- [16] G. Chen, H. Huang, and Z. Xiang, "Experimental investigation on the anticollision performance of corrugated steel-reinforced composites for bridge piers," *Shock and Vibration*, vol. 2021, Article ID 5847559, 17 pages, 2021.
- [17] Z. Zeng, Y. Xiao, W. Wang, Z. Huang, W. Wei, and S. B. Houdou, "Research on dynamic performance of CRTS type slab ballastless track under long-term service," *Materials*, vol. 15, no. 6, Article ID 15062033, 2022.
- [18] P. Xu, C. Qu, S. Yao, C. Yang, and A. Wang, "Numerical optimization for the impact performance of a rubber ring buffer of a train coupler," *Machines*, vol. 9, no. 10, p. 225, Article ID 9100225, 2021.

- [19] Y. Lu, Q. Shi, Y. Chen, W. Zheng, and Y. Zhou, "Response suppression of multiple hinged floating structures by using rubber cushion," *Shock and Vibration*, vol. 2021, Article ID 1208336, 17 pages, 2021.
- [20] X. Lei, "Inductive method of landing shock data of aero engine and shock characteristics analysis," *Journal of Vibration, Measurement & Diagnosis*, vol. 41, no. 3, pp. 601–605+628, 2021.
- [21] Z. Luo, K. Xie, B. Zou, M. Jiang, and W. Zheng, "Structural dynamic response of a shield tunnel under aircraft taxiing load," *Shock and Vibration*, vol. 2021, Article ID 3999948, 9 pages, 2021.
- [22] P. Li, Y. Li, and L. Sun, "Research on anti-impact scaling test method for supporting structure of large equipment," *Nuclear Power Engineering*, vol. 43, no. 4, pp. 99–105, 2022.
- [23] D. Huang, "Dynamic analysis of construction protective formworks subject to an impact load," *HKIE Transactions*, vol. 20, no. 2, pp. 133–140, 2013.
- [24] H. M. Hilber, T. J. R. Hughes, and R. L. Taylor, "Improved numerical dissipation for time integration algorithms in structural dynamics," *Earthquake Engineering & Structural Dynamics*, vol. 5, no. 3, pp. 283–292, 1977.
- [25] X. Zhao, *Dynamic Response Algorithm Design and Analysis with Controllable High Frequency Dissipation Based on Discrete Control Theory*, Qingdao University of Technology, Qingdao, China, 2021.
- [26] Z. Zhang and Z. Chen, *Naval Ship Vibration*, Science Press, Beijing, China, 2021.